Fast Count—Regulated OSEM Reconstruction With Adaptive Resolution Recovery

Pieter E. B. Vaissier*, Marlies C. Goorden, Aaron B. Taylor, and Freek J. Beekman, *Senior Member, IEEE*

Abstract—Ordered subsets expectation maximization (OSEM) is widely used to accelerate tomographic reconstruction. Speed-up of OSEM over maximum likelihood expectation maximization (MLEM) is close to the number of subsets (NS). Recently we significantly increased the speed-up achievable with OSEM by specific subset choice (pixel-based OSEM). However, a high NS can cause undesirable noise levels, quantitative inaccuracy or even disappearance of lesions in low-activity image regions, while a low NS leads to prohibitively long reconstructions or unrecovered details in highly active regions. Here, we introduce count-regulated OSEM (CROSEM) which locally adapts the effective NS based on the estimated amount of detected photons originating from individual voxels. CROSEM was tested using multi-pinhole SPECT simulations and *in vivo* imaging. With the maximum NS set to 128, CROSEM attained acceleration factors close to 128 in high-activity regions and kept quantitative accuracy in low-activity regions close to that of MLEM. At equal cold-lesion contrast in high-activity regions, CROSEM exhibited lower noise than MLEM in low-activity regions. CROSEM is a fast and stable alternative to OSEM, preventing excessive image noise and quantitative errors in low-activity regions while achieving high-resolution recovery in structures with high activity uptake.

Index Terms—Image reconstruction, positron emission tomography (PET), reconstruction algorithms, single photon emission computed tomography (SPECT).

I. INTRODUCTION

IN RECENT YEARS, statistical iterative algorithms have become the method of choice for reconstructing single photon emission computed tomography (SPECT) and positron emission tomography (PET) images [1]–[5]. Additionally, significant interest is being shown in accelerated versions of these algorithms for X-ray computed tomography [6]–[13]. Compared to analytical reconstruction methods, statistical iterative methods have been shown to 1) be more robust to statistical noise, 2) be applicable to complex detector-and collimator geometries, and 3) allow better modeling of the physical detection process, which can be used to correct for several image-degrading effects. Of these iterative methods, maximum likelihood expectation maximization (MLEM, [14], [15]) has become the gold standard, mostly due to its consistent and predictable convergence behavior, non-negativity constraint, and ease of implementation.

Despite the ever increasing computer speed, MLEM remains computationally costly as the size of system matrices is also increasing over time. This trend is driven by, on the one hand, the use of more refined models of photon transport which are desired for better resolution recovery and quantitatively accurate images [16], and on the other hand by the demand for finer voxel grids to accommodate the increasing resolution of modern (preclinical) SPECT and PET [17]. A major breakthrough that has led to the widespread application of statistical iterative algorithms in medical image reconstruction was the introduction of block-iterative methods. These methods use ordered subsets (OS) of the projection data in each sub-iteration of the algorithm to accelerate resolution recovery. This principle was applied to MLEM to yield the ordered subsets expectation maximization algorithm (OSEM, [18]). Despite the fact that OSEM has no theoretical convergence proof and that the approach is heuristically motivated, OSEM is currently the most widely used iterative reconstruction method in emission tomography: OSEM is fast, easy to implement and has been shown to yield acceptable images for a large variety of imaging studies. Studies have shown that for parallel hole-collimated SPECT, OSEM provides almost the same reconstructed images as MLEM, when the number of subsets (NS) is not too high [19], [20] and that the acceleration factor is roughly proportional to the NS [18], [19]. In most OSEM implementations, each subset contains a number of complete SPECT projections. It was recently shown that it can be more advantageous to use pixel-based subset schemes (pixel-based OSEM; POSEM, [21]). These schemes deviate from traditional subset schemes in that subsets do not consist of grouped projection views, rather the detector pixels in each subset are spread out in a regular pattern over the entire detector and therefore each subset contains detector pixels from all projection views. This way, subset balance does not deteriorate as fast as with traditional subset schemes as the NS increases. In a number of cases POSEM could achieve acceleration factors that were an order of magnitude higher than those of traditional OSEM when applied to multi-pinhole SPECT.

*P. E. B. Vaissier is with the Department of Radiation Science and Technology, Delft University of Technology, 2628 CN Delft, The Netherlands (e-mail: p.e.b.vaissier@tudelft.nl).

M. C. Goorden is with the Department of Radiation Science and Technology, Delft University of Technology, 2628 CN Delft, The Netherlands (e-mail: m.c.goorden@tudelft.nl).

A. B. Taylor is with the Bindley Bioscience Center, Purdue University, West Lafayette, IN 47907 USA (e-mail: abtaylor@purdue.edu).

F. J. Beekman is with the Department of Radiation Science and Technology, Delft University of Technology, 2628 CN Delft, The Netherlands, and with MI-Labs B.V., 3584 CX Utrecht, The Netherlands, and also with UMC Utrecht Brain Center Rudolf Magnus, 3584 CG Utrecht, The Netherlands (e-mail: f.j.beekman@tudelft.nl).
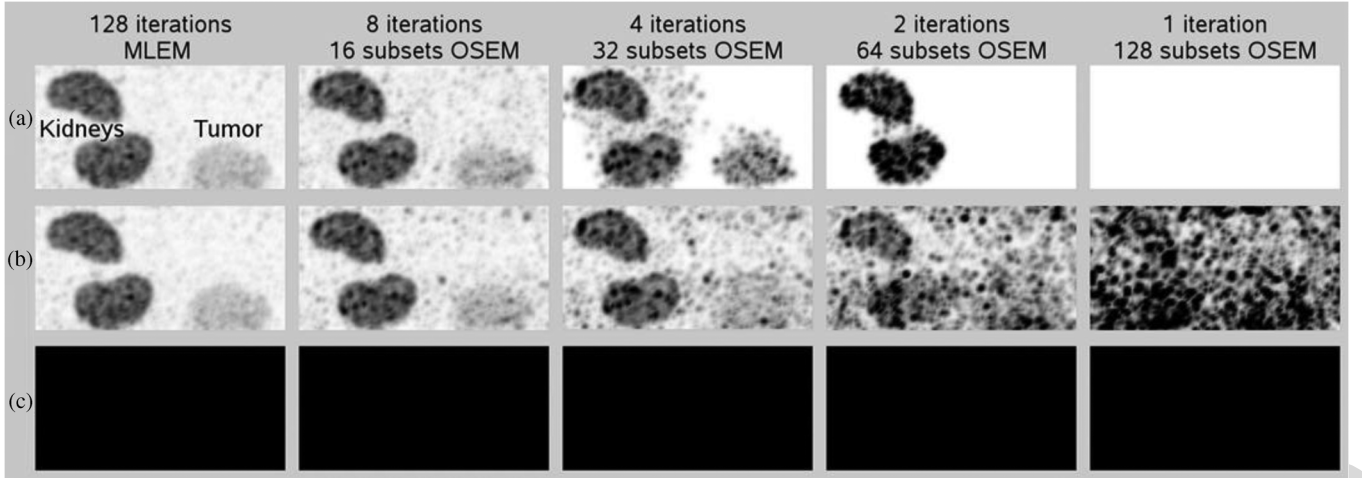
Fig. 1. MIPs of SPECT reconstructions of mouse with tumor (16.7 MBq $^{99\,m}\mathrm{Tc}$-prostate-specific-membrane-antigen-targeted ($^{99\,m}\mathrm{Tc}$-PSMA) radioligand [22], scanned for 32 min starting 4 h postinjection). The grayscale is the same for all MIPs. MLEM reconstructions and OSEM reconstructions for several NS: (a) if voxel updates to zero activity are allowed, (b) if voxel updates to zero activity are not allowed, and (c) if detector pixels with no counts are simply excluded from the measured data.

This paper addresses and solves a shortcoming of OSEM that, to our knowledge, has not been reported previously in literature. The problems that can rise when OSEM is operated at a high NS are illustrated in Fig. 1(a). This figure shows maximum-intensity-projections (MIPs) of MLEM and OSEM reconstructions of a SPECT scan of a tumor-bearing mouse that was injected with 16.7 MBq $^{99\,m}\mathrm{Tc}$-prostate-specific-membrane-antigen-targeted ($^{99\,m}\mathrm{Tc}$-PSMA) radioligand [22] and was scanned for 32 min, starting 4 h postinjection. From the MLEM reconstruction (Fig. 1(a), left) it is clear that the tracer accumulated in the kidneys and to a much lesser extent in the tumor. In OSEM reconstructed images activity in more and more voxels was erased as the NS increased; e.g., for OSEM with 64 subsets activity in the tumor completely disappeared and for OSEM with 128 subsets activity in the entire image was erased. Note that the grayscale is the same for all MIPs in Fig. 1. These major reconstruction artifacts occur if a large fraction of the (small) detector pixels in each subset contain no counts. In such cases, it may happen that a subset exists in which all detector pixels that occur in the update term of a certain voxel do not contain any counts and, as a consequence, the activity in this voxel will be updated to zero in the sub-iteration that uses this subset. Due to the multiplicative nature of the OSEM update step the activity in this voxel will then remain zero, even if detector pixels in other subsets that are used to update the voxel do contain counts. As shown in Fig. 1(a), this can lead to the permanent erasure of activity. Furthermore, because OSEM strives to make re-projected activity consistent with measured projections, extra activity may accumulate in surrounding voxels. The occurrence of these effects becomes more likely for a decreasing number of counts and/or an increase of the NS.

To prevent these reconstruction artifacts fewer subsets could be used. However, since there is no general rule for selecting a low enough NS to avoid quantification errors and tumor/lesion detection loss in regions with low activity, one needs to always select a low NS and ends up with 1) very time consuming reconstructions and noisy low-activity regions due to the high number of iterations that is required to achieve a high resolution in high-activity regions, or 2) a low resolution in the entire image if a low number of iterations is performed to save reconstruction time. As a simple solution, one may also consider to only perform nonzero activity updates [Fig. 1(b)] or to simply exclude detector pixels that contain no counts [Fig. 1(c)]. Although these two strategies may work for moderate/high count (PET) data, we have tried these options and found reconstructions full of artifacts when applied to (low-count) pinhole-SPECT. Note that with pinhole-SPECT it may regularly occur that the majority of the detector pixels contain no counts. Therefore, leaving out the detector pixels that contain no counts means not using a substantial amount of the detector pixels. These pixels do contain information about the likelihood of a certain activity distribution as they indicate that the voxels that project onto them probably contain low activities. Therefore, simply excluding these pixels resulted in severe overestimation of the activity in all images presented in Fig. 1(c) (i.e., overall black MIPs).

Alternatively, the low-count induced reconstruction problems of Fig. 1(a) can be prevented by the use of an algorithm that adapts its acceleration speed (i.e., the NS) automatically and locally depending on local activity estimates. Such a type of EM algorithm was already introduced in [23] and referred to as statistically regulated EM (StatREM). StatREM utilizes the concepts of statistically adaptive subset formation and spatially adaptive voxel updates. StatREM closely resembles OSEM in that subsets of the measured projection data are used for voxel updates. However, while OSEM updates all voxels in each sub-iteration, StatREM only updates a voxel if it passes a statistical hypothesis test which considers the differences between the simulated and measured counts for those detector pixels that occur in the update term of a certain voxel; i.e., the system matrix elements (sensitivities) corresponding to these voxel-pixel combinations are nonzero. If the test passes (the difference is significant) the conclusion is drawn that this voxel is at least partially responsible for the mismatch between the simulated and measured data and the voxel is updated. It was shown that Sta-

tREM accelerated recovery of spatial resolution in high-activity image regions, while noise artifacts in low-activity regions were reduced. However, the voxel-wise test used within StatREM does not take into account how likely it is that counts in a certain detector pixel originate from the voxel under consideration. For example, a pixel may only be slightly sensitive to the photons originating from a certain voxel (i.e., low value of the system matrix element) and therefore the voxel may not be expected to contribute much to that detector pixel. Or, alternatively, a voxel may be estimated to have a low activity and therefore it will not contribute many counts to any detector pixel. This may result in suboptimal images, as we will show later in this paper. To overcome these problems we introduce a new Count-Regulated version of the OSEM algorithm (CROSEM): CROSEM also uses adaptive subset formation and spatially adaptive voxel updates by means of a voxel-wise test, however the test used within CROSEM is based on the estimated contribution (i.e., counts) of individual voxels to the detector pixels taking into account 1) the probability that a photon from a certain voxel ends up being detected in a certain detector pixel (i.e., the value of the system matrix element) and, 2) the estimated activity level of the voxel under consideration.

The aim of this paper is to introduce and validate CROSEM and to show that it automatically achieves a locally adapted resolution-noise trade-off, prevents erasure of activity and noise over-amplification in low-activity image regions while still enabling fast resolution recovery in high-activity regions. We compare CROSEM to MLEM, OSEM and StatREM for multi-pinhole SPECT and illustrate the benefit of CROSEM with reconstructions of *in vivo* data.

II. MATERIALS AND METHODS

A. Image Reconstruction Algorithms

MLEM: In this study, we used an implementation of MLEM according to [14] as a basis for OSEM, StatREM and CROSEM. The MLEM update equation is given by

$$\widetilde{a}_i^{(k)} = \frac{\widetilde{a}_i^{(k-1)}}{\sum_j M_{ij}} \sum_j M_{ij} \frac{p_j}{\widetilde{p}_j^{(k)}} \tag{1}$$

$$\widetilde{p}_j^{(k)} = \sum_i M_{ij} \widetilde{a}_i^{(k-1)}. \tag{2}$$

Here, $\widetilde{a}_i^{(k)}$ is the estimated activity in voxel i at the kth iteration, p_j and $\widetilde{p}_j^{(k)}$ are the measured and estimated (simulated) number of gamma photon counts in detector pixel j with an energy that lies within the selected photopeak window and M_{ij} is the system matrix element representing the probability that a photon emitted from voxel i is detected in detector pixel j. In this study the start image is a cylinder with uniform activity.

OSEM: OSEM uses the same equation as MLEM to update the image estimate but for each update only a subset of the projection data is used. Such an update step is called a sub-iteration. Only after all subsets have been traversed sequentially, a single OSEM iteration is defined to be completed (full iteration). The OSEM image update is defined by

$$\widetilde{a}_i^{(k,l)} = \frac{\widetilde{a}_i^{(k,l-1)}}{\sum\limits_{j \in S_l} M_{ij}} \sum\limits_{j \in S_l} M_{ij} \frac{p_j}{\widetilde{p}_j^{(k,l)}}. \tag{3}$$

In (3), $\widetilde{a}_i^{(k,l)}$ is the activity in voxel i after processing subset l in iteration k and S_l contains the detector pixels of subset l.

StatREM: We implemented StatREM with voxel-wise statistical hypothesis testing according to [23]. The test (paired-sample two-tailed t-test) considers the differences between the measured and simulated counts for the detector pixels that occur in the update term of a certain voxel and assumes that these differences are normally distributed. To make sure that the statistical test is also meaningful in the first iteration, the initial (uniform) start image is scaled such that the total activity in the image is consistent with the total number of counts in the projection data.

The test statistic $TT_i^{(k,l)}$ for voxel i in sub-iteration (k,l) is calculated as follows: the sum of weighted differences $d_i^{(k,l)}$ between the measured and estimated detector counts that occur in the correction term of voxel i in sub-iteration (k,l) is defined as

$$d_i^{(k,l)} = \sum\limits_{\substack{j \in S_l \\ M_{ij} \neq 0}} \frac{\left(p_j - \widetilde{p}_j^{(k,l)}\right)}{\sqrt{\widetilde{p}_j^{(k,l)}}}. \tag{4}$$

The variable $tt_i^{(k,l)}$ is a running sum that increases each sub-iteration by $d_i^{(k,l)}$

$$tt_i^{(k,l)} = tt_i^{(k,l-1)} + d_i^{(k,l)}. \tag{5}$$

The test statistic $TT_i^{(k,l)}$ is then calculated by

$$TT_i^{(k,l)} = \frac{1}{\sqrt{U}} \left(tt_i^{(k,l)}\right). \tag{6}$$

Note that $d_i^{(k,l)}$ in (4) only includes those detector pixels that occur in the update term of voxel i (i.e., $M_{ij} \neq 0$) and U in (6) is the number of detector pixels that are considered in the calculation of $tt_i^{(k,l)}$. At the same time, both the correction term $C_i^{(k,l)}$ and the normalization term $N_i^{(l)}$, which respectively multiply and normalize the voxel value in each update, are also running sums: each sub-iteration, a new correction and normalization term are defined, which are the correction and normalization term acquired in the current sub-iteration (k,l) added to the terms acquired in all previous sub-iterations of the current iteration k that have been traversed since the last update of voxel i

$$C_i^{(k,l)} = C_i^{(k,l-1)} + \sum\limits_{j \in S_l} M_{ij} \frac{p_j}{\widetilde{p}_j^{(k,l)}} \tag{7}$$

$$N_i^{(l)} = N_i^{(l-1)} + \sum\limits_{j \in S_l} M_{ij}. \tag{8}$$

If the t-test demonstrates a statistically significant difference between the measured and simulated projection counts for a specified statistical test level α (i.e., the value of the test statistic

$TT_i^{(k,l)}$ that is calculated in (6) lies outside the confidence interval for a confidence level of $100(1-\alpha)\%$, the null-hypothesis that the current activity estimates resulted in the measured data is rejected and voxel i is updated

$$\widetilde{a}_i^{(k,l)} = \frac{\widetilde{a}_i^{(k,l-1)}}{N_i^{(l)}} C_i^{(k,l)}. \tag{9}$$

After the update, $tt_i^{(k,l)}$, $C_i^{(k,l)}$ and $N_i^{(l)}$ are reset to zero. Note that StatREM might still allow activity updates to zero: in case the test passes (i.e., there is a significant difference between the simulated and measured projection counts) and $C_i^{(k,l)}$ is zero (i.e., zero measured counts in the pixels that contributed to $C_i^{(k,l)}$) voxel i is updated to zero.

CROSEM: Like StatREM, CROSEM uses update equations (7)–(9) and only updates voxels that pass a test. However, with CROSEM a different test is performed that is based on the current activity estimate of the voxel under consideration. In order to obtain an initial estimate of each voxel's activity the CROSEM algorithm commences with a single MLEM iteration

$$\widetilde{a}_i^{(1)} = \frac{\widetilde{a}_i^{(0)}}{\sum_j M_{ij}} \sum_j M_{ij} \frac{p_j}{\widetilde{p}_j^{(1)}}. \tag{10}$$

Here, $\widetilde{a}^{(0)}$ and $\widetilde{p}^{(1)}$ are respectively the (uniform) start image and its estimated projection. Further iterations are, like StatREM, performed, using a fixed (high) NS, in this work denoted by $\mathrm{NS}^{\mathrm{max}}$. Starting from the second iteration, in each sub-iteration one determines the number of counts that a certain voxel is expected to contribute to the detector pixels of the current subset based on the current activity estimate of the voxel. This number, added to the number of counts that this voxel was expected to contribute to all previous subsets since its last update, determines if the voxel will be updated or not: the voxel is only updated when this number is higher than a certain count threshold value (CTV). To put this in equations, consider the test for voxel i in sub-iteration (k,l): define $\widetilde{t}_i^{(k,l)}$ as the estimated (simulated) number of photons originating from voxel i that is detected in the detector pixels of subset l

$$\widetilde{t}_i^{(k,l)} = \sum_{j \in S_l} M_{ij} \widetilde{a}_i^{(k,l-1)}. \tag{11}$$

The value $T_i^{(k,l)}$ is a running sum that increases each sub-iteration by $\widetilde{t}_i^{(k,l)}$

$$T_i^{(k,l)} = T_i^{(k,l-1)} + \widetilde{t}_i^{(k,l)}. \tag{12}$$

Once the running test value $T_i^{(k,l)}$ exceeds the CTV and the correction term in (7) is nonzero ($C_i^{(k,l)} > 0$), the contribution of voxel i to the projection data is deemed high enough to justify an update and the voxel is updated as in (9). Note that requiring $C_i^{(k,l)} > 0$ serves as an extra safety measure in preventing the voxel activity from being updated to zero, which might occur if the voxel's activity estimate is much higher than the actual activity (e.g., activity estimates in early iterations), while there are no measured counts in the detector pixels that occur in its correction term ($C_i^{(k,l)} = 0$). After the update, $T_i^{(k,l)}$, $C_i^{(k,l)}$,

and $N_i^{(l)}$ are reset to zero. Furthermore, if voxel i was updated in a certain sub-iteration, but was not updated in all consecutive sub-iterations of the full iteration, $T_i^{(k,l)}$, $C_i^{(k,l)}$, and $N_i^{(l)}$ are carried into the next full iteration $k+1$ until the test passes. However, if a voxel was not updated over a number of sub-iterations equal to $\mathrm{NS}^{\mathrm{max}}$, an update for that voxel is forced by using detector pixels from all subsets. Thus, the number of individual voxel updates in a full CROSEM iteration can range from 1 (MLEM-like update) up to $\mathrm{NS}^{\mathrm{max}}$. With CROSEM, the activity in a voxel can still be updated to zero if in all subsets none of the detector pixels that are associated with that voxel contain any counts. In such case, MLEM would also update the corresponding voxel activity to zero. Since CROSEM automatically reduces the effective NS to update low-activity regions in an image, CROSEM can always be used with a high $\mathrm{NS}^{\mathrm{max}}$ irrespective of the details of a scan.

To make the CTV independent of the reconstructed voxel size, the CTV is in units of the number of (estimated) counts per milliliter. Before image reconstruction commences, the CTV is scaled to the number of counts per voxel, a number that depends on voxel size. The CTV is closely related to the count levels in the image as it sets a minimum to the number of counts that a voxel has to contribute to the projection data before an update of that voxel is performed. Low-count image voxels are less likely to meet this requirement each sub-iteration; only after projection pixels from a number of subsets are added together to form a larger subset this requirement is met. The contribution from a high-activity voxel to each subset of the projection data can be larger than the CTV for every subset and therefore these voxels can be updated every sub-iteration. To illustrate how CROSEM updates voxels depending on their activity estimate, assume that CROSEM reconstruction is performed on 0.5 mm voxels with the $\mathrm{NS}^{\mathrm{max}} = 128$ and the CTV $= 40\,000$ counts/ml. These reconstruction parameters imply that each voxel has to contribute at least five counts to the projection data before it is updated (the volume of a single voxel is 1/8000 ml; a CTV of $40\,000$ counts/ml corresponds to a CTV of five counts/voxel). As a result, a voxel that contributed ≥ 5 counts to the projection data of each subset would be updated every sub-iteration, while a voxel that contributed less than five counts to the entire projection data would be updated only once every full iteration, thereby using detector pixels from all subsets.

Note that OSEM requires that each voxel is seen by every subset. If not, reconstruction artifacts arise because voxels that are not seen in a certain subset have zero-valued normalization terms in that subset. In most OSEM implementations this is overcome by not updating these voxels or by allocating zero activity to these voxels, however these strategies may still result in artifacts. CROSEM inherently prevents these artifacts by its requirement that a voxel must contribute counts to the subset with which it is updated, which implies that normalization terms are never zero.

In this work, OSEM, StatREM, and CROSEM were applied with pixel-based subset schemes [21] and StatREM and CROSEM were always operated with $\mathrm{NS}^{\mathrm{max}} = 128$. In the remainder of this work, k iterations MLEM is denoted as "$k$it MLEM," k iterations OSEM applied with NS subsets as "$k$it OSEM-NS," k iterations StatREM with a statistical test level
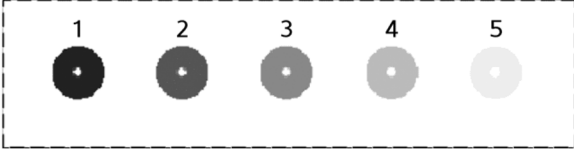
Fig. 2. Longitudinal slice through center of digital image quality phantom containing five activity-filled spheres (diameter = 10 mm) with spherical cold-lesions (diameter =2 mm) at their centers. Each consecutive sphere contains a factor 10 lower activity. Image is presented on log-grayscale.

α as "$k$it StatREM-α" and k iterations CROSEM with a CTV β as "$k$it CROSEM-β."

B. Focusing Multi-Pinhole SPECT Scanner

In this study we used the U-SPECT-II/CT scanner (MI-Labs B.V., Utrecht, The Netherlands) which is dedicated to ultra-fast, ultra-sensitive and ultra-high resolution imaging of rodents [17]. It has three large-area gamma cameras [595 mm $\times$ 472 mm NaI(Tl)] and each camera is subdivided into pixels of about 1 mm $\times$ 1 mm. The energy-and spatial resolution of these cameras are about 10% and 3.5 mm full-width at half-maximum (FWHM), respectively. The cameras are placed in a triangular configuration with a focusing multi-pinhole collimator positioned at the center of the scanner. In the present study a collimator tube for mouse-sized animals was used [17], both for simulations and experiments. The 75 pinholes in this collimator all have an opening angle of 30° and together create a field-of-view (FOV) that encompasses the entire collimator tube diameter (44 mm) and has the shape of an hourglass. A central part of the FOV (CFOV; transaxial diameter 12 mm, axial length 8 mm) is sampled by all pinholes simultaneously and within the CFOV complete data is readily obtained. Imaging of larger volumes is performed by translating the animal through the collimator along a spiral trajectory [24]. Evaluations show that the spatial resolution that can be achieved with this collimator can reach 0.4 mm (0.6 mm pinholes), while <0.3 mm can be achieved when using smaller pinholes. The system matrix M is obtained through PSF measurements, modeling and interpolations [25]. The image reconstruction algorithm exploits all projections, acquired from all positions of the animal inside the collimator, simultaneously, rather than stitching together reconstructions of sub-volumes that each correspond to a single position of the animal inside the collimator. This method of combined acquisition and reconstruction is called the scanning focus method (SFM, [26]).

C. Digital Image Quality Phantom SPECT Simulation

To evaluate the quantitative accuracy and the rate of convergence (the iterative recovery of image features) of MLEM, OSEM, StatREM, and CROSEM, SPECT simulations of a digital image quality phantom were performed. The cylindrical phantom was mouse-sized (Fig. 2; diameter 24 mm, length 100 mm) and it contained five spheres (diameter 10 mm) filled with different activity concentrations. To simulate both low- and high-count projection data, every consecutive sphere contained a 10 times lower activity concentration (highest for sphere 1, lowest for sphere 5). While such large differences in activity concentration might not commonly occur in a single scan, it

may represent count levels from different scans with a large difference in activity concentration and/or scan time (since the number of counts depends on both activity and scan time). The center of each sphere contained a small spherical cold-lesion for contrast measurements (diameter 2 mm, no activity). The activity concentration in the remainder of the phantom was uniform and 10 times lower than the activity concentration inside sphere 5. To mimic a realistic continuous activity distribution, the voxel size of the phantom was 0.15 mm, half the size of the voxels in the reconstructed images.

The fast simulator that was used in this study is based on ray tracing to account for resolution-degrading effects of pinhole diameter and pinhole edge penetration [27], [28]. The radionuclide that was simulated is $^{99\text{ m}}$Tc (140 keV gamma photons). The intrinsic resolution of the detectors and detection efficiency for 140 keV gamma photons were set in correspondence with experimental data to a Gaussian response with a FWHM of 3.5 mm and a value of 89%, respectively. The simulator was used to simulate noiseless phantom projection data and to pre-calculate the system matrix. From the noiseless projections, 10 noise realizations were created by generating Poisson statistics, taking into account total administered activity and scan duration (57.7 MBq and 60 min, respectively, resulting in 19.5 M counts in each noise realization).

All noise realizations were reconstructed with MLEM, with OSEM for a range of NS (NS = 16, 32, 64, and 128 subsets), with StatREM for a range of statistical test levels (NS$^{\text{max}}$ = 128; statistical test level=0.01, 0.05, 0.1, and 0.2) and with CROSEM for a range of CTVs (NS$^{\text{max}}$ = 128; CTV = 40 k, 20 k, 10 k, and 5 k counts/ml). All reconstructions were postfiltered with a 3D-Gaussian kernel with a FWHM of 0.4 mm.

To evaluate the quantitative accuracy of each algorithm, a mean reconstructed image was determined by averaging images over all noise realizations. From this mean image longitudinal image slices through the transaxial centers of the spheres were made. Furthermore, reconstructed activities inside 11-mm-diameter spherical volumes-of-interest (VOIs; centered on the spheres) were determined in each of the noise realizations. This resulted in a mean and standard deviation of the reconstructed activity in each sphere, expressed in terms of percentage reconstructed activity relative to the true sphere activity.

To assess differences in iterative convergence speed and compare contrast and noise characteristics between the algorithms, cold-lesion contrast and noise were calculated. The average contrast inside a sphere at iteration k was defined to be the cold-lesion contrast at that iteration averaged over all noise realizations, with the contrast in noise realization r at iteration k being defined as

$$\text{Contrast}^{(r,k)} = \frac{\left\langle A_{\text{hot}}^{(r,k)} \right\rangle - \left\langle A_{\text{cold}}^{(r,k)} \right\rangle}{\left\langle A_{\text{hot}}^{(r,k)} \right\rangle}. \tag{13}$$

Here, $\left\langle A_{\text{cold}}^{(r,k)} \right\rangle$ is the average reconstructed activity per voxel inside a 1-mm-diameter spherical VOI centered on the cold-lesion and $\left\langle A_{\text{hot}}^{(r,k)} \right\rangle$ is the average reconstructed activity per voxel in a spherical annulus surrounding the cold-lesion (inner and outer diameter 4 and 8 mm, respectively).

As a measure of the noise in each sphere, the normalized standard deviation inside the cold-lesion region was averaged over all noise realizations, with the noise in noise realization r at iteration k being defined as

$$\text{Noise}^{(r,k)} = \frac{1}{\left\langle A_{\text{cold}}^{(r,k)} \right\rangle} \sqrt{\frac{\sum_{q=1}^{Q} \left(A_{\text{cold}}^{(r,k)}(q) - \left\langle A_{\text{cold}}^{(r,k)} \right\rangle \right)^2}{Q - 1}}. \tag{14}$$

Here, $A_{\text{cold}}^{(r,k)}(q)$ is the reconstructed activity in voxel q inside the cold-lesion VOI, which consisted of Q voxels. If due to reconstruction artifacts (i.e., erasure of activity) contrast and/or noise for one of the spheres could not be calculated, contrast and/or noise for that sphere were defined to be zero.

D. In Vivo SPECT

To illustrate the performance of CROSEM on experimental data, *in vivo* data was reconstructed. We compared these reconstructions to MLEM reconstructions (gold standard) and also performed OSEM and StatREM reconstructions. Considering the performance of StatREM and CROSEM in the phantom SPECT simulation study, a test level of 0.05 (StatREM) and a CTV of 20 k counts/ml (CROSEM) were used and eight iterations were performed with both algorithms. The number of OSEM iterations at which OSEM reconstructions were compared to MLEM reconstructions was based on the rule of thumb that performing k iterations OSEM with NS subsets leads to a resolution and contrast approximately equivalent to applying $k{*}NS$ iterations MLEM [18], [19]. From this rule of thumb follows that 128 MLEM iterations are required to compare MLEM to OSEM with up to 128 subsets (16, 32, 64, and 128 subsets were tested).

Scan of a Tumor-Bearing Mouse: A 20 g male mouse was inoculated in the shoulder with 22Rv1 human prostatic carcinoma cells. The tumor developed for three weeks and the mouse was then intravenously injected with 16.7 MBq of a proprietary $^{99\,m}\text{Tc}$-prostate-specific-membrane-antigen-targeted ($^{99\,m}\text{Tc}$-PSMA) radioligand [22]. Four hours postinjection the mouse was sacrificed and a SPECT scan was performed for 32 min. For the generation of the projection data a 20% energy window was set around the $^{99\,m}\text{Tc}$-photopeak. Images were reconstructed on 0.375 mm voxels and the images were postfiltered with a 3D-Gaussian kernel with a FWHM of 1.0 mm. From these images MIPs, image slices and image slice profiles were generated. Furthermore, VOIs were selected for the kidneys and the tumor from the MLEM reconstructed image. Using these VOIs reconstructed activities were determined in the OSEM, StatREM, and CROSEM images, expressed as percentages of the activities that were reconstructed with MLEM. This experiment was conducted in accordance with Purdue University Animal Care and Use Committee guidelines.

Bone-Scan of a Mouse: A 30 g male mouse was anesthetized with isoflurane. An amount of 189 MBq $^{99\,m}\text{Tc}$-hydroxymethylene diphosphonate ($^{99\,m}\text{Tc}$-HDP) was injected in the tail vein. Scanning started right before radioligand injection and the mouse was scanned for 60 min in frames of 1 min. Low-count projection data was obtained from the last scan
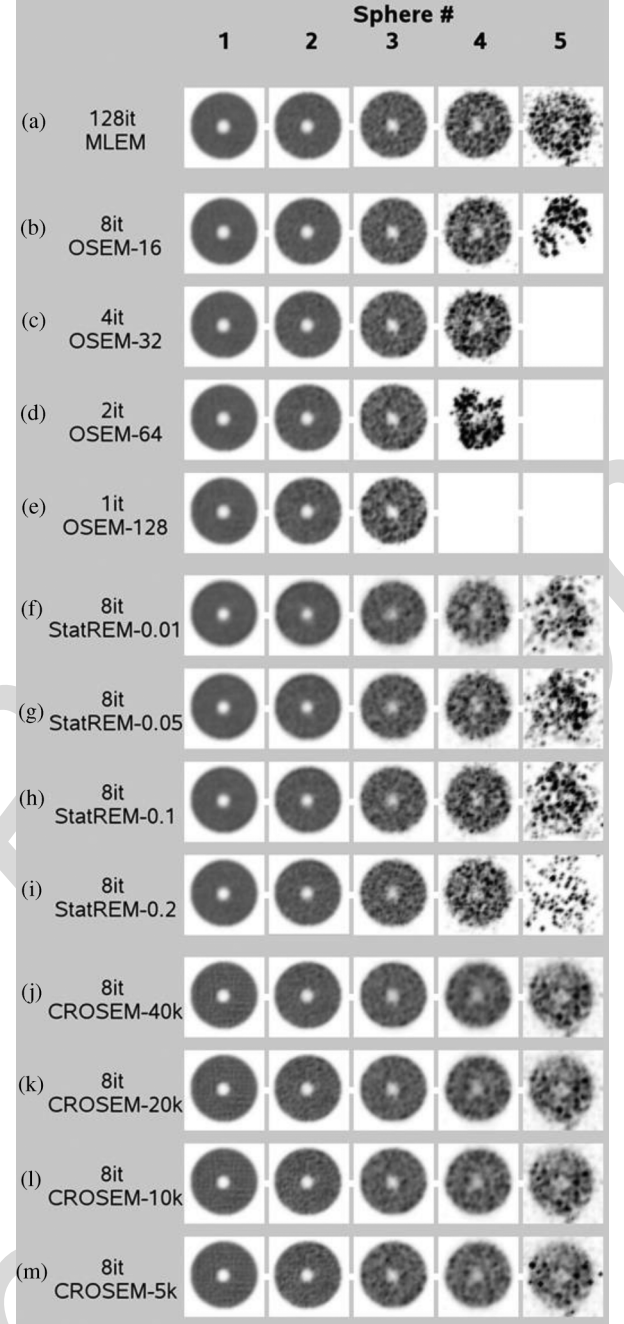

Fig. 3. Reconstructions (average over 10 noise realizations) of simulated image quality phantom scan (57.7 MBq $^{99\,m}\text{Tc}$, 60 min scan time). Longitudinal image slices through centers of spheres (different grayscale per sphere) for (a) MLEM, (b)–(e) OSEM for several NS, (f)–(i) StatREM for several test levels, and (j)–(m) CROSEM for several CTVs.

frame using a 25% energy window set around the $^{99\,m}\text{Tc}$-photopeak. Images were reconstructed on 0.4 mm voxels and the images were postfiltered with a 3D-Gaussian kernel with a FWHM of 1.0 mm. From the same scan, projection data containing more counts was obtained by summing the projection data of the final 50 min of the scan. Images from this high-count data were reconstructed on 0.2 mm voxels and the images were postfiltered with a 3D-Gaussian kernel with a FWHM of 0.4 mm. For all reconstructions MIPs were generated. Furthermore, VOIs were selected for the bladder and a section of the

TABLE I
RECONSTRUCTED ACTIVITIES (% OF GOLD STANDARD)

Algorithm	Sphere #				
	1	2	3	4	5
128it MLEM	99.8±0.0	99.9±0.1	99.7±0.3	99.4±1.2	88.6±2.5
8it OSEM-16	99.8±0.1	99.8±0.3	99.3±1.2	99.1±3.0	72.4±7.3
4it OSEM-32	99.8±0.2	100.0±0.5	98.9±1.3	101.3±4.4	0.0±0.0
2it OSEM-64	99.8±0.2	99.9±0.5	98.4±2.0	77.6±4.7	0.0±0.0
1it OSEM-128	99.9±0.3	100.0±0.7	99.9±2.8	0.0±0.0	0.0±0.0
8it StatREM-0.01	99.9±0.0	99.5±0.1	96.5±0.3	86.9±0.8	68.8±9.1
8it StatREM-0.05	99.9±0.0	99.8±0.1	98.3±0.2	95.0±1.0	82.1±10.4
8it StatREM-0.1	100.0±0.0	100.0±0.1	99.4±0.3	98.6±1.7	85.3±14.0
8it StatREM-0.2	100.0±0.0	100.3±0.1	100.6±0.4	94.5±2.8	41.1±14.4
8it CROSEM-40k	99.9±0.3	99.6±0.4	98.2±0.5	96.7±1.1	85.8±2.2
8it CROSEM-20k	99.9±0.3	99.8±0.4	98.0±0.8	97.1±1.2	85.6±2.3
8it CROSEM-10k	99.9±0.3	99.8±0.6	97.8±1.1	96.1±1.6	84.8±2.4
8it CROSEM-5k	100.0±0.3	99.9±0.6	97.9±1.4	94.4±2.3	84.7±2.6

spine from the MLEM reconstructed images. Using these VOIs reconstructed activities were determined in the OSEM, StatREM and CROSEM images, expressed as percentages of the activities that were reconstructed with MLEM. This experiment was conducted following protocols approved by the Animal Research Committee of the University Medical Center Utrecht.

III. RESULTS

A. Digital Image Quality Phantom SPECT Simulation

Fig. 3 shows longitudinal slices (thickness: 1.2 mm) through the mean reconstructed phantom images (average over 10 noise realizations) for (a) MLEM, (b)–(e) OSEM for several NS, (f)–(i) StatREM for several test levels, and (j)–(m) CROSEM for several CTVs. The MLEM reconstructed image is shown for 128 iterations, OSEM reconstructions are shown at an iteration number approximately equivalent to 128 MLEM iterations and both StatREM and CROSEM reconstructions are shown for iteration #8. To adequately visualize all spheres with strongly varying activity between them, the spheres are displayed one by one with a different grayscale for each sphere.

For MLEM as well as for all tested CROSEM reconstructions, all spheres were clearly visible. However, OSEM reconstructions increasingly deviated from MLEM as the NS increased; more and more activity in spheres 4 and 5 was erased until their activity completely disappeared in the reconstruction with 128 subsets. For all tested StatREM reconstructions spheres 1–4 were clearly visible, but the reconstructions of sphere 5 showed considerable artifacts as activity in many voxels was erased in the reconstructions of the individual noise realizations, although these artifacts were found to be not as severe as in the OSEM reconstructions.

Table I shows for each algorithm the percentage of reconstructed activity in spheres 1–5 relative to the true activity. All algorithms recovered >95% of the activity in spheres 1–3. For sphere 4, MLEM still performed well in quantifying the activity and CROSEM performed almost as well for all tested CTVs. OSEM showed increasing quantification errors for reconstruction with an increasing NS. StatREM preformed approximately as good as CROSEM, except for the strictest (lowest) test level.

For sphere 5, MLEM and CROSEM still performed very similar in terms of quantification, whereas all of the tested OSEM reconstructions performed significantly worse; for OSEM-32, OSEM-64, and OSEM-128 even all activity was erased. All tested StatREM reconstructions showed severe quantification errors in terms of large standard deviations, which increased with less strict (higher) test levels. For the lowest and highest test level not only high standard deviations were observed but also large errors in mean reconstructed activity. These results indicate that for quantification of activity, CROSEM performs significantly better than OSEM and StatREM and that CROSEM almost matches MLEM.

Fig. 4 shows average contrast versus average noise (average over 10 noise realizations) inside sphere 1 and sphere 5 for OSEM, StatREM and CROSEM. The graphs also display the corresponding MLEM curves (solid lines).

For OSEM, contrast and noise characteristics inside sphere 1 were found to be comparable to MLEM [Fig. 4(a)]. The contrast recovery speed-up of OSEM over MLEM in sphere 1 was found to be approximately equal to the NS, which can be deduced from the MLEM and OSEM iteration numbers at approximately equal contrast and noise which are also displayed in the figure. For sphere 5, all OSEM reconstructions showed large artifacts and the average noise could therefore not be calculated and was defined to be zero [Fig. 4(b)]. Furthermore, because of these artifacts all OSEM reconstructions resulted in zero contrast, except for OSEM-16 where an unrealistically high contrast was calculated. Fig. 4(b) only shows the first iteration for each tested OSEM since contrast-noise characteristics did not improve at later iterations.

For sphere 1, all tested StatREM reconstructions resulted in a lower contrast than MLEM at approximately equal noise levels [Fig. 4(c)]. It can also be seen that higher (less strict) test levels resulted in faster convergence in high-activity regions: e.g., 23 it StatREM-0.01, 15 it StatREM-0.05, 13 it StatREM-0.1, and 10 it StatREM-0.2 were required to obtain a contrast and noise level approximately equivalent to 384 it MLEM. For all test levels of StatREM, activities in many voxels of sphere 5 were erased in individual noise realizations and the average noise could therefore not be calculated and
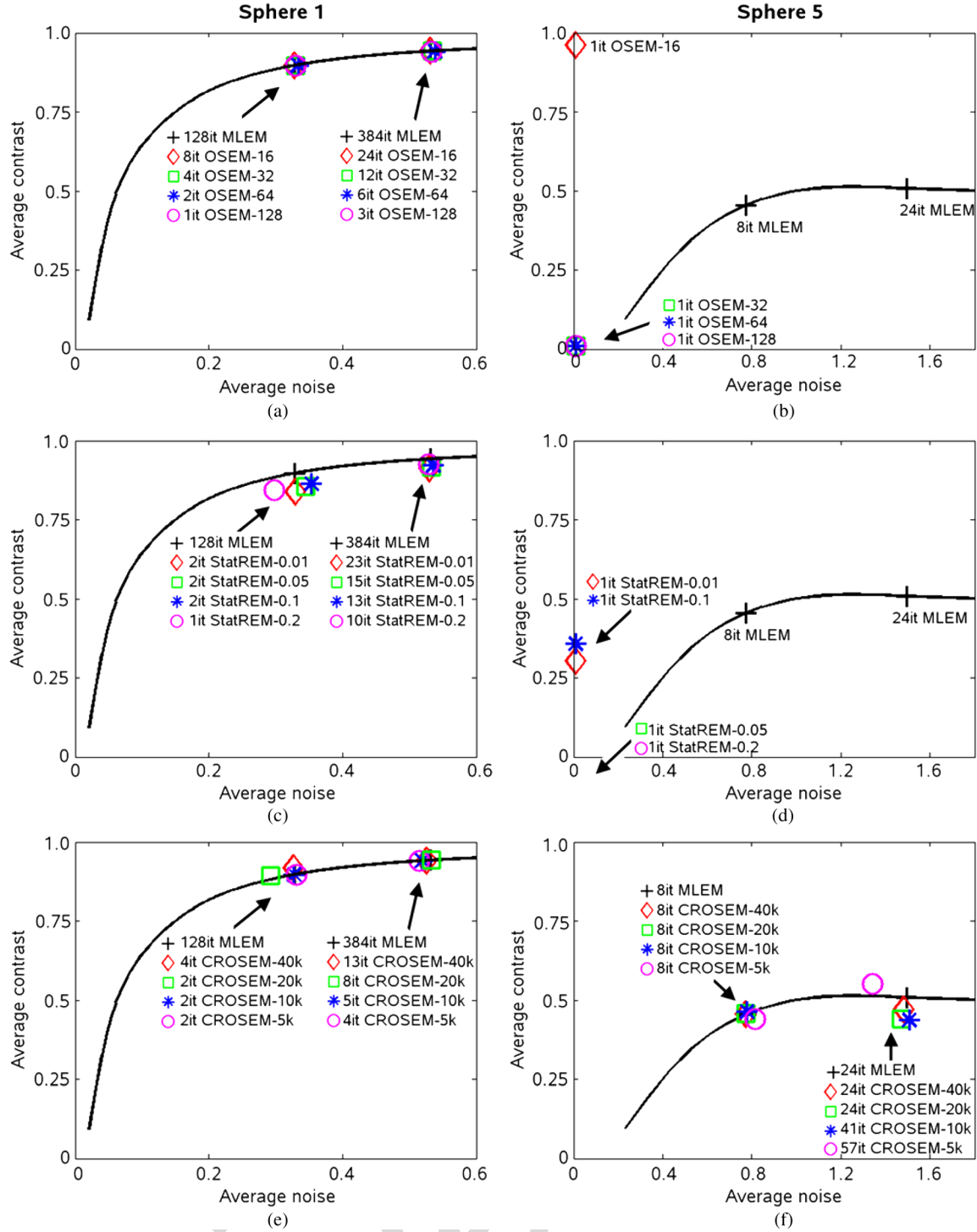
Fig. 4.   Graphs of average contrast versus average noise (average over 10 noise realizations) in sphere 1 (left graphs) and sphere 5 (right graphs) for (a), (b) OSEM, (c), (d) StatREM, and (e), (f) CROSEM. Graphs also show corresponding MLEM curves (solid lines).

was defined to be zero [Fig. 4(d)]. Furthermore, negative contrasts were found for some test levels of StatREM, because in some of the noise realizations the average activity in the cold lesion was higher than the average activity in the hot region. Fig. 4(d) only shows the first iteration for each test level of StatREM since contrast-noise characteristics did not improve at later iterations. For CROSEM, contrast and noise characteristics inside sphere 1 were found to be comparable to MLEM

[Fig. 4(e)]. CROSEM attained high speed-up over MLEM for sphere 1: e.g., 4 it CROSEM-40 k, 2 it CROSEM-20 k, 2 it CROSEM-10 k, and 2 it CROSEM-5 k resulted in a contrast and noise level approximately equivalent to 128 it MLEM (Note that the first CROSEM iteration was an ordinary MLEM iteration so there was no speed-up over MLEM in this iteration). It can also be seen that a lower CTV resulted in faster convergence in high-activity regions: e.g., 13 it CROSEM-40 k,
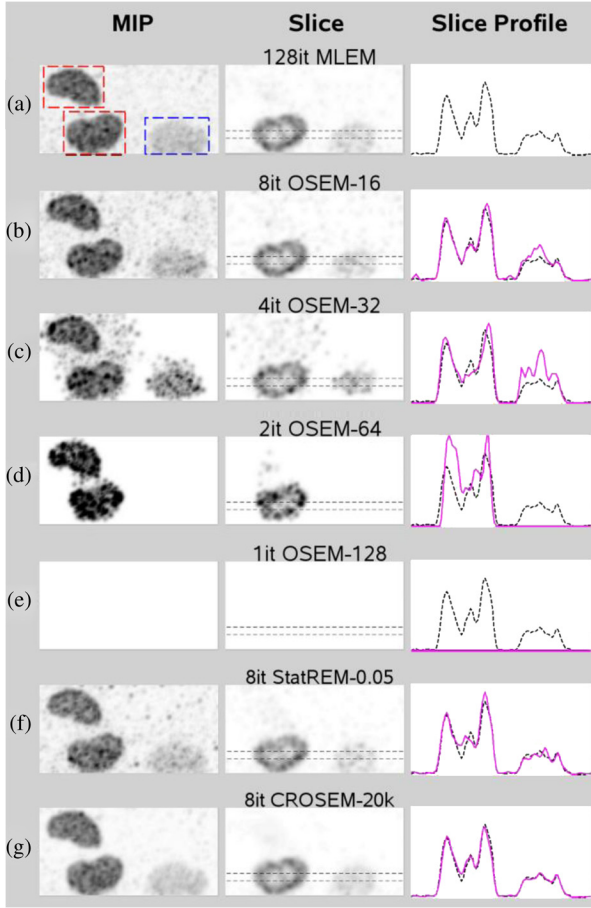
Fig. 5. MIPs, slices, and profiles of same SPECT scan, as shown in Fig. 1. Image profiles of (a) MLEM (dashed black line) are compared to (b)–(e) OSEM for several NS, (f) StatREM-0.05, and (g) CROSEM-20 k (solid magenta lines): CROSEM-20 k deviates very little from MLEM. MIP in (a) indicates VOIs for kidneys (red) and tumor (blue).

8 it CROSEM-20 k, 5 it CROSEM-10 k, and 4 it CROSEM-5 k were required to obtain a contrast and noise level approximately equivalent to 384 it MLEM. For sphere 5 [Fig. 4(f)], CROSEM-40 k and CROSEM-20 k behaved approximately MLEM-like in terms of contrast and noise characteristics and speed, although their contrast at higher iterations was slightly worse than MLEM. CROSEM operated with CTVs lower than 20 k counts/ml behaved approximately MLEM-like in early iterations, however at higher iterations more iterations than MLEM were required to arrive at a similar contrast-noise as MLEM, which indicates that these CTVs are suboptimal (e.g., 41 it CROSEM-10 k resulted in a similar contrast-noise as 24 it MLEM). Fig. 4(e) and (f) clearly illustrates that CROSEM achieves a local contrast-noise tradeoff: CROSEM attained high speed-up factors over MLEM inside high-activity regions (sphere 1) and at the same time no speed-up over MLEM in very low-activity regions (sphere 5): 8 it CROSEM-20 k resulted in a contrast and noise equivalent to 384 it MLEM inside sphere 1 and resulted in a contrast and noise equivalent to 8 it MLEM inside sphere 5.

These results indicate that CROSEM (for CTVs $\geq$20 k counts/ml) can achieve very high speed-up over MLEM and that CROSEM is comparable to MLEM in terms of local

TABLE II
RECONSTRUCTED ACTIVITIES (% OF 128 it MLEM RECONSTRUCTED ACTIVITIES)

Algorithm	Kidneys	Tumor
8it OSEM-16	102.4	97.4
4it OSEM-32	102.8	86.5
2it OSEM-64	92.3	0.0
1it OSEM-128	0.0	0.0
8it StatREM-0.05	98.3	102.0
8it CROSEM-20k	98.8	98.4

TABLE III
RECONSTRUCTED ACTIVITIES (% OF 128 it MLEM RECONSTRUCTED ACTIVITIES)

	1-min scan		50-min scan	
Algorithm	Bladder	Spine	Bladder	Spine
8it OSEM-16	99.5	88.3	100.0	101.0
4it OSEM-32	99.3	40.9	100.1	101.1
2it OSEM-64	99.9	11.3	100.6	101.4
1it OSEM-128	89.3	0.0	98.4	104.3
8it StatREM-0.05	98.8	89.6	99.1	98.0
8it CROSEM-20k	96.3	94.7	98.5	100.4

contrast and noise characteristics, whereas OSEM and StatREM resulted in severe reconstruction artifacts in low-activity regions.

B. In Vivo SPECT

Scan of a Tumor-Bearing Mouse: Fig. 5 shows the reconstructed SPECT images of a tumor-bearing mouse for (a) MLEM, (b)–(e) OSEM for several NS, (f) StatREM-0.05, and (g) CROSEM-20 k. Similar to the phantom studies discussed above, activity in more and more voxels was being erased in OSEM reconstructions as the NS increased: for OSEM-128 activity inside the kidneys and tumor even completely disappeared. The image profiles (thickness and width: 1.875 mm) clearly show deviations between MLEM (dashed black line) and OSEM (solid magenta lines), which became larger for an increase in the NS. The StatREM-0.05 image and profile are much closer to the MLEM image and profile, although the MIP looks noisier and the profile deviates in some places. The MIP of the CROSEM-20 k reconstruction appears to be less noisy than the one of StatREM-0.05 and the profile of CROSEM-20 k almost perfectly matches the one of MLEM.

Table II shows the percentages of reconstructed activity in the kidneys and the tumor [VOIs indicated in Fig. 5(a)] obtained with OSEM, StatREM-0.05, and CROSEM-20 k relative to the activities obtained with MLEM. StatREM-0.05 and CROSEM-20 k show the smallest deviations from MLEM, while for OSEM the deviations from MLEM became larger for an increase in the NS.

Bone-Scan of a Mouse: Fig. 6 shows the results for 1-min and 50-min mouse bone-scan reconstructions with (a) MLEM, (b)–(e) OSEM for several NS, (f) StatREM-0.05, and (g) CROSEM-20 k. For the OSEM reconstructions of the 1-min scan (Fig. 6(b)–(e), left) large parts of the image were erased as the NS increased: in the image that was reconstructed with OSEM-128 only high-activity regions of the liver and bladder had nonzero activity. StatREM-0.05 resulted in a very noisy
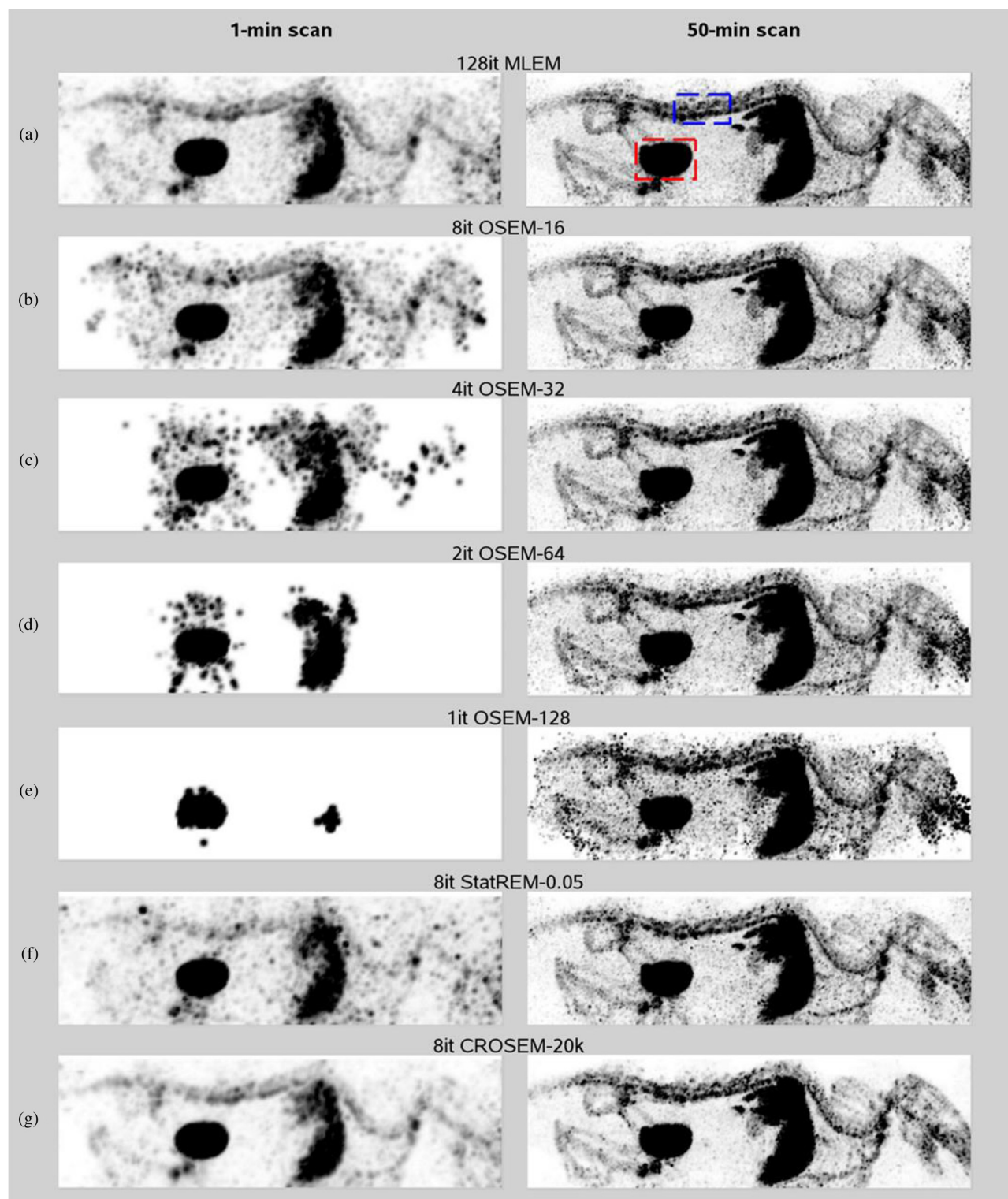
Fig. 6.   MIPs of mouse bone-scan reconstructions (189 MBq $^{99\,m}$Tc-HDP) of 1-min (left) and 50-min (right) scans for (a) MLEM, (b)–(e) OSEM for several NS, (f) StatREM-0.05, and (g) CROSEM-20 k. Right MIP in (a) indicates VOIs for bladder (red) and spine (blue).

reconstruction and bony structures are only vaguely visible (Fig. 6(f), left). In contrast, CROSEM-20 k clearly shows all the structures that are visible in the MLEM image (Fig. 6(g), left).

The OSEM reconstructions of the 50-min scan (Fig. 6(b)–(e), right) also show artifacts as the NS increased; the MIPs look in-creasingly noisy and again activity in parts of the OSEM-128 image was erased (e.g., parts of the jaw and tail), although these artifacts were not as severe as in the OSEM reconstructions of the 1-min scan. The StatREM-0.05 reconstruction (Fig. 6(f), right) looks very similar to the one of MLEM. The CROSEM-20 k reconstruction (Fig. 6(g), right) shows a high level of detail in

high-activity regions and less noisy low-activity regions compared to MLEM.

Table III shows the percentages of reconstructed activities in the bladder and a part of the spine [VOIs are indicated in Fig. 6(a)] relative to the activities obtained with 128 it MLEM for the 1-min and 50-min acquisitions. For the 1-min scan reconstructions OSEM increasingly underestimated the activity in the spinal region as the NS increased, while for the 50-min scan all tested OSEM performed similar to MLEM. For the 1-min scan reconstruction, StatREM-0.05 resulted in underestimation of the activity in the spine by about 10%, while for the 50-min scan StatREM-0.05 deviated little from MLEM. For the 1-min scan, CROSEM-20 k underestimated the activities maximally about 5%, while for the 50-min scan CROSEM-20 k recovered about the same activity as MLEM.

IV. Discussion

In this study, we have shown that CROSEM applied with a single setting of the reconstruction parameters (NS^{max} and CTV) achieves high image resolution in highly active regions while still yielding quantitatively accurate images in regions with low activity uptake. In this study we have also shown that OSEM reconstruction could result in major reconstruction artifacts in regions with low activity and that these artifacts become more severe as the NS increases. Although StatREM generally outperformed OSEM in terms of quantifying activity in low-activity regions, we still found significant reconstruction artifacts in these regions.

With CROSEM, the number of voxel updates is nonuniform over the image since it depends on the reconstructed activity distribution and, as a result, a spatially variant regularization is imposed: high-activity regions tend to recover a higher spatial resolution and contrast to better match the measured projections, whereas a high resolution can not be achieved in low-activity regions and therefore less updates, resulting in more smoothness, can be preferable in these regions to avoid amplification of noise. However, users need to be aware of nonuniform spatial resolution since this could introduce errors into quantitative comparisons since partial volume effects will depend on local activity levels.

In this study, we tested CROSEM for image reconstruction of SPECT data. In general, PET has higher sensitivity than SPECT and low-count induced OSEM artifacts may therefore be less important in PET. On the other hand, dose reduction in PET is still desirable and many new screening protocols or longitudinal studies would come into reach when very low-dose PET can be performed. We believe that for such low-dose PET (or dynamic PET studies with low counts per time frame) CROSEM may also improve contrast-noise characteristics over OSEM. Furthermore, as long as CROSEM is operated with balanced subsets, we see no reason why CROSEM could not be applied with (traditional) projection-based subsets which are mostly used in clinical SPECT and PET.

The extra reconstruction time that is needed for a full CROSEM iteration over an MLEM iteration is small: e.g., the reconstruction time of the mouse bone-scan acquired over 1 min (voxel size: 0.4 mm) was 1.5 min per iteration for MLEM (performed on four AMD processors using in total 16 cores; Opteron 6174, 2.19 GHz), while CROSEM required only <15 s extra time per full iteration. Note that this is extra time per iteration and that CROSEM requires many fewer iterations than MLEM to achieve a high resolution in highly active image regions.

Besides CROSEM, other accelerated reconstruction algorithms may also prevent erasure of low-activity image regions. One way to accelerate reconstruction and prevent activity erasure is by applying a power factor in the MLEM update step to obtain an accelerated MLEM algorithm [29]. However, the speed-up of this algorithm over MLEM is still limited. There are also convergent OS methods which can be divided into relaxed-and incremental OS methods. A well-known relaxed OS algorithm is RAMLA [30]. RAMLA uses relaxation within a modified version of OSEM. Since there are no general rules for finding relaxation schedules that result in high reconstruction speed-up factors over MLEM, a separate optimization study is required, and a comparison between the performance of optimized RAMLA and optimized CROSEM remains a topic for future research. A well-known incremental OS algorithm is COSEM [31]. COSEM does not require a user-specified relaxation schedule; however, the speed-up of COSEM lies between MLEM and optimized RAMLA. Faster convergence may be achieved by starting with OSEM and switching to a convergent OS algorithm at later iterations. However, for low-count (multi-pinhole) SPECT, a low number of subsets can already result in activity erasure in a large fraction of the voxels.

V. Conclusion

CROSEM is a fast and stable alternative to OSEM that prevents excessive image noise and quantitative errors in low-activity regions while achieving high-resolution recovery in structures with high activity uptake. A single setting of the reconstruction parameters (NS^{max} and CTV) leads to images with high resolution where possible and good quantitative accuracy for all imaging studies presented here in which we covered a wide range of doses and activity distributions. In addition our results clearly indicate that CROSEM can help prevent users having to compromise between resolution and quantitative accuracy.

References

[1] F. J. Beekman, H. W. A. M. De Jong, and S. Van Geloven, "Efficient fully 3-D iterative SPECT reconstruction with Monte Carlo based scatter compensation," *IEEE Trans. Med. Imag.*, vol. 21, no. 8, pp. 867–877, Aug. 2002.

[2] B. F. Hutton, H. M. Hudson, and F. J. Beekman, "A clinical perspective of accelerated statistical reconstruction," *Eur. J. Nucl. Med.*, vol. 24, pp. 797–808, 1997.

[3] R. Leahy and C. Byrne, "Recent developments in iterative image reconstruction for PET and SPECT," *IEEE Trans. Med. Imag.*, vol. 19, no. 4, pp. 257–260, Apr. 2000.

[4] R. M. Leahy and J. Y. Qi, "Statistical approaches in quantitative positron emission tomography," *Stat. Comput.*, vol. 10, pp. 147–165, 2000.

[5] J. Qi and R. M. Leahy, "Iterative reconstruction techniques in emission computed tomography," *Phys. Med. Biol.*, vol. 51, pp. 541–578, 2006.

[6] F. J. Beekman and C. Kamphuis, "Ordered subset reconstruction for x-ray CT," *Phys. Med. Biol.*, vol. 46, no. 7, pp. 1835–1844, Jul. 2001.

[7] B. De Man, J. Nuyts, P. Dupont, G. Marchal, and P. Suetens, "An iterative maximum-likelihood polychromatic algorithm for CT," *IEEE Trans. Med. Imag.*, vol. 20, no. 10, pp. 999–1008, Oct. 2001.

[8] H. Erdogan and J. A. Fessler, "Ordered subsets algorithms for transmission tomography," *Phys. Med. Biol.*, vol. 44, pp. 2835–2851, 1999.

[9] J. S. Kole and F. J. Beekman, "Evaluation of the ordered subset convex algorithm for cone-beam X-ray CT," *Phys. Med. Biol.*, vol. 50, no. 4, pp. 613–623, 2005.

[10] S. H. Manglos, G. M. Gagne, A. Krol, F. D. Thomas, and R. Narayanaswamy, "Transmission maximum-likelihood reconstruction with ordered subsets for cone-beam CT," *Phys. Med. Biol.*, vol. 40, no. 7, pp. 1225–1241, 1995.

[11] J. Nuyts, B. De Man, P. Dupont, M. Defrise, P. Suetens, and L. Mortelmans, "Iterative reconstruction for helical CT: A simulation study," *Phys. Med. Biol.*, vol. 43, pp. 729–737, 1998.

[12] W. Zbijewski and F. J. Beekman, "Efficient Monte Carlo based scatter artifact reduction in cone-beam micro-CT," *IEEE Trans. Med. Imag.*, vol. 25, no. 7, pp. 817–827, Jul. 2006.

[13] W. Zbijewski, M. Defrise, M. A. Viergever, and F. J. Beekman, "Statistical reconstruction for x-ray CT systems with non-continuous detectors," *Phys. Med. Biol.*, vol. 52, no. 2, pp. 403–418, Jan. 2007.

[14] K. Lange and R. Carson, "EM reconstruction algorithms for emission and transmission tomography," *J. Comp. Assist. Tomogr.*, vol. 8, pp. 306–316, 1984.

[15] L. A. Shepp and Y. Vardi, "Maximum likelihood reconstruction for emission tomography," *IEEE Trans. Med. Imag.*, vol. 1, no. 2, pp. 113–122, Oct. 1982.

[16] B. F. Hutton, I. Buvat, and F. J. Beekman, "Review and current status of SPECT scatter correction," *Phys. Med. Biol.*, vol. 56, no. 14, pp. R85–R112, Jul. 2011.

[17] F. Van der Have, B. Vastenhouw, R. M. Ramakers, W. Branderhorst, J. O. Krah, C. Ji, S. G. Staelens, and F. J. Beekman, "U-SPECT-II: An ultra-high-resolution device for molecular small-animal imaging," *J. Nucl. Med.*, vol. 50, no. 4, pp. 599–605, Mar. 2009.

[18] H. M. Hudson and R. S. Larkin, "Accelerated image reconstruction using ordered subsets of projection data," *IEEE Trans. Med. Imag.*, vol. 13, no. 4, pp. 601–609, Dec. 1994.

[19] C. Kamphuis, F. J. Beekman, and M. A. Viergever, "Evaluation of OS-EM vs. ML-EM for 1D, 2D and fully 3D SPECT reconstruction," *IEEE Trans. Nucl. Sci.*, vol. 43, no. 3, pp. 2018–2024, Jun. 1996.

[20] D. S. Lalush and B. M. Tsui, "Performance of ordered-subset reconstruction algorithms under conditions of extreme attenuation and truncation in myocardial SPECT," *J. Nucl. Med.*, vol. 41, pp. 737–744, 2000.

[21] W. Branderhorst, B. Vastenhouw, and F. J. Beekman, "Pixel-based subsets for rapid multi-pinhole SPECT reconstruction," *Phys. Med. Biol.*, vol. 55, no. 7, pp. 2023–2034, Apr. 2010.

[22] S. A. Kularatne, Z. Zhou, J. Yang, C. B. Post, and P. S. Low, "Design, synthesis, preclinical evaluation of prostate-specific membrane antigen targeted (99 m) Tc-radioimaging agents," *Mol. Pharmaceutics*, vol. 6, no. 3, pp. 790–800, Jun. 2009.

[23] D. J. Kadrmas, "Statistically regulated and adaptive EM reconstruction for emission computed tomography," *IEEE Trans. Nucl. Sci.*, vol. 48, no. 3, pp. 790–798, Jun. 2001.

[24] P. E. B. Vaissier, M. C. Goorden, B. Vastenhouw, F. van der Have, R. M. Ramakers, and F. J. Beekman, "Fast spiral SPECT with stationary gamma-cameras and focusing pinholes," *J. Nucl. Med.*, vol. 53, no. 8, pp. 1292–1299, Aug. 2012.

[25] F. Van der Have, B. Vastenhouw, M. Rentmeester, and F. J. Beekman, "System calibration and statistical image reconstruction for ultra-high resolution stationary pinhole SPECT," *IEEE Trans. Med. Imag.*, vol. 27, no. 7, pp. 960–971, Jul. 2008.

[26] B. Vastenhouw and F. Beekman, "Submillimeter total-body murine imaging with U-SPECT-I," *J. Nucl. Med.*, vol. 48, no. 3, pp. 487–93, 2007.

[27] M. Gieles, H. W. A. M. de Jong, and F. J. Beekman, "Monte Carlo simulations of pinhole imaging accelerated by kernel-based forced detection," *Phys. Med. Biol.*, vol. 47, pp. 1853–1867, 2002.

[28] M. C. Goorden, F. van der Have, R. Kreuger, and F. J. Beekman, "An efficient simulator for pinhole imaging of PET isotopes," *Phys. Med. Biol.*, vol. 56, no. 6, pp. 1617–1634, Mar. 2011.

[29] D. Hwang and G. L. Zeng, "Convergence study of an accelerated ML-EM algorithm using bigger step size," *Phys. Med. Biol.*, vol. 51, no. 2, pp. 237–252, Jan. 2006.

[30] J. Browne and A. R. De Pierro, "A row-action alternative to the EM algorithm for maximizing likelihoods in emission tomography," *IEEE Trans. Med. Imag.*, vol. 15, no. 5, pp. 687–699, Oct. 1996.

[31] I. T. Hsiao, A. Rangarajan, P. Khurd, and G. Gindi, "An accelerated convergent ordered subsets algorithm for emission tomography," *Phys. Med. Biol.*, vol. 49, pp. 2145–56, 2004.